

## Article

# Layered Binder-Free C/Si Anodes for Li Ion Batteries

Rumen I. Tomov <sup>1,\*</sup>, Dmitry Yarmolich <sup>2</sup> and Vasant Kumar <sup>1</sup>

<sup>1</sup> Department of Materials Science and Metallurgy, University of Cambridge, Cambridge CB2 3QZ, UK; rvk10@cam.ac.uk

<sup>2</sup> Plasma App Ltd., Building R18 Rutherford Appleton Laboratory, Harwell Oxford Innovation Campus, Didcot OX11 0QX, UK

\* Correspondence: rit21@cam.ac.uk

## Abstract

Novel high-energy, binder-free, and solvent-free carbon–silicon layered composite anodes were manufactured using an industrially scalable Virtual Cathode Deposition (VCD) technique. The deposition process transforms commercial graphite target material into carbon polymorph (CALIB) layers, interposed with silicon layers deposited *in situ* from a silicon source, thereby forming high-capacity anodes for Li ion batteries. Composite CALIB-C/Si<sub>4</sub> anodes with a layered architecture exhibited a first-cycle specific capacity of over 1550 mAh g<sup>-1</sup> at 0.1 A g<sup>-1</sup> and retained a capacity of ~1080 mAh g<sup>-1</sup> at a 1 A g<sup>-1</sup> rate after 200 cycles. Detailed structural characterisation revealed a disordered carbon matrix encompassing nanosized sp<sup>2</sup>-bonded carbon clusters (average size ~20 nm), cross-linked by a network of sp<sup>3</sup>-bonded atomic sites, with predominant mesoporosity and high surface area. The silicon layers were found to consist of an amorphous Si matrix with embedded nanocrystalline components, emulating the growth mode of the CALIB buffer. The presence of the mesoporous carbon matrix accommodated the stress caused by the alloying/de-alloying of silicon nanolayers, thereby alleviating the pulverisation effect and preserving the structural integrity of the composite. The initial performance and capacity decay of the anodes were found to depend on the thickness of the CALIB-C buffer interlayers.

**Keywords:** carbon; silicon; Li ion; anode; layered; binder free



Academic Editor: Shaokun Chong

Received: 30 September 2025

Revised: 16 October 2025

Accepted: 21 October 2025

Published: 30 October 2025

**Citation:** Tomov, R.I.; Yarmolich, D.; Kumar, V. Layered Binder-Free C/Si Anodes for Li Ion Batteries. *Batteries* **2025**, *11*, 400. <https://doi.org/10.3390/batteries1110400>

**Copyright:** © 2025 by the authors. Licensee MDPI, Basel, Switzerland. This article is an open access article distributed under the terms and conditions of the Creative Commons Attribution (CC BY) license (<https://creativecommons.org/licenses/by/4.0/>).

## 1. Introduction

Major efforts have been made in recent years to develop a new generation of Li-ion batteries (LIBs) that meet the growing demand for reliable energy storage and address impending global environmental challenges. LIBs have played an essential role in the accelerating the portable electronic devices market [1,2] and have enabled commercially viable electrical vehicles technology, as well as balancing stationary storage solutions to mitigate smart grids intermittency. Further sustainable commercialisation of LIBs will require a substantial enhancement of both gravimetric and volumetric energy density, safer operation, and faster charging. The carbon footprint of LIB fabrication technology also needs to be minimised using lower-cost, non-toxic, and abundant materials.

Currently, graphite is the commercial anode material of choice. It is abundant, low-cost, and offers several advantageous properties, such as low working potential, high electrical conductivity, and improved safety compared to metallic lithium anodes.

However, the intercalation capacity of graphitic type anodes is restricted by the stoichiometry of LiC<sub>6</sub>, reaching a theoretical maximum of 372 mAh g<sup>-1</sup> [3,4]. Substantially higher specific capacities have been reported for composite carbonaceous anodes based

on the utilisation of various nanocarbon forms with different dimensional properties (1D—nanotubes, 2D—graphene-like materials, and nanosheets or 3D—templated mesoporous carbons). Some notable results have been summarised in several comprehensive review papers [5–8]. The observed performance improvements are commonly attributed to the large surface-to-volume ratios and higher surface activities of the nano-engineered electrodes, as well as, in some cases, extended electronic pathways and faster diffusion channels. These combinations contribute to enhanced specific capacity and improved charge-discharge rates. However, the use of carbon nanomaterials has also demonstrated some specific disadvantages [9,10]:

- (i) Lower packing density achieved with the available fabrication techniques and hence lower volumetric capacity.
- (ii) Irreversible consumption of Li ions due to formation of extended solid electrolyte interphase (SEI).
- (iii) High production costs.

Further attempts to increase the anode capacity have been made by combination of intercalation (carbon) and alloying (silicon) materials. Silicon is a low-cost, abundant, and non-toxic material having a high theoretical capacity ( $3579 \text{ mA h g}^{-1}$  for  $\text{Li}_{3.75}\text{Si}$ ) and a low discharge voltage of 0.2–0.3 V vs. Li/Li<sup>+</sup>. These advantages have led to an intensive research effort into its potential application as anode for Li ion batteries. However, a number of fundamental issues have hindered its practical application:

- (i) Substantial volume change during alloying/de-alloying reaching 290% with formation of crystalline  $\text{Li}_{3.75}\text{Si}$  at alloying voltages below 50 mV<sub>Li</sub>.
- (ii) Low intrinsic electronic conductivity of Si ( $\sim 10^{-3} \text{ S cm}^{-1}$ ).
- (iii) Low ionic conductivity (Li ion diffusion coefficient  $\sim 10^{-13} \text{ cm}^2 \text{ s}^{-1}$ ) compared to hard carbon ion conductivity (Li ion diffusion coefficient  $\sim 10^{-9} \text{ cm}^2 \text{ s}^{-1}$ ).

The alloying of Si proceeds through several amorphous phase changes—a-Si → a-Li<sub>2</sub>Si → a-Li<sub>3.5</sub>Si—before forming a crystalline c-Li<sub>3.75</sub>Si phase at approximately 300–250 mV, ~120–50 mV, and <50 mV<sub>Li</sub>, respectively. The repeated swelling and contraction cause mechanical pulverisation of the electrode material and unstable cyclic re-formation of the solid electrolyte interphase (SEI), leading to progressively higher irreversible capacity loss, low initial Coulombic efficiency (CE), as well as loss of electrical contact with both the current collector and within the electrode itself. However, it was discovered that the detrimental pulverisation effect of silicon is particle size dependant. Silicon nanoparticles with diameter bellow a critical size of 150 nm have been shown to be able to accommodate the strain of lithiation/delithiation cycling, thereby alleviating cracking or fracturing [11].

Alternatively, it has been demonstrated that, in nano-engineered C/Si nanocomposites, the carbon can buffer the strain caused by the cyclic volume variation as well as stabilize the formation of SEI by isolating the nano-silicon from the electrolyte [12,13]. Large number of Si/C composites with different nano dimensions have been experimented with in recent years by many researchers reporting impressive achievements [14,15]. It was demonstrated that porous C/Si composites could provide adequate void space to buffer Si expansion, an excellent electron conductive network and fast Li<sup>+</sup> diffusion pathways thus leading to high specific capacities and enhanced rate performances. For example, Yanli Chen et al. [16] reported an Si/CNFs@rGO electrode with a  $2608 \text{ mAh g}^{-1}$  first-cycle capacity and  $1055 \text{ mAh g}^{-1}$  reversible capacity after 130 cycles at a  $0.1 \text{ A g}^{-1}$  rate. The electrodes were prepared by an electrospinning/electrostatic self-assembly/hydrothermal dehydration method. The amount of Si in Si/CNFs@rGO composite was estimated at ~40 wt. percentage. In another study, Qingrui Pan et al. [17] fabricated a micro-sized silicon @ carbon @ graphene spherical composite electrode by a spray drying–calcination

process. They obtained an initial specific capacity of  $1599 \text{ mAh g}^{-1}$  (at  $0.2 \text{ A g}^{-1}$  rate) and a retained capacity of  $1517 \text{ mAh g}^{-1}$  in cycle 100 (at a  $0.2 \text{ A g}^{-1}$  rate). Fei Dou et al. [18] made a systematic classification of the Si/C composite anodes based on 0D, 1D, 2D, and 3D electrode architectures, citing similar or higher reversible capacities with high retention. Yongling An et al. [19], from Shandong University (P. R. China), demonstrated the fabrication of a three-dimensional porous silicon confined by homogeneous N-doped carbon nano-sheet frameworks by the thermo-chemical treatment of commercial bulk precursors and the subsequent evaporation of by-products. Such anode delivered cycling with 95.68% capacity retention for up to 4000 cycles at  $5 \text{ A g}^{-1}$ . Similarly produced two-dimensional L-Si/C anode delivered more than 80% capacity retention after 3200 cycles with superior rate performance [20].

Substantial efforts have been directed towards the optimisation of amorphous (nanocrystalline) Si/C multilayered anodes. For amorphous Si films, the critical thickness of the Si layer has been reported to be between 100 and 200 nm [21]. However, both chemomechanical modelling and experimental studies have demonstrated that nanosized silicon and carbon coatings could fracture if the internal stresses are sufficiently high [22]. It has also been shown that the pulverisation effect in ultrathin ( $<10 \text{ nm}$ ) alternating carbon and silicon layers may be attributed to the formation of  $\text{Li}_{3.75}\text{Si}$  phase. Therefore, suppression of the pulverisation effect was found to depend on the relative thicknesses of the silicon and carbon layers as well as the lithiation cut-off voltage [23,24].

In densely packed multilayered Si/C anodes prepared by PVD or CVD methods, the liquid electrolyte is normally prevented from deep penetration before the electrode is cracked. In such anodes, the cracking occurs during the initial de-lithiation step [25]. Zhao et al. [24] reported that by optimizing the C/Si thickness ratio one could achieve the C/Si multilayer electrode to crack into relatively uniform blocks with stable SEI formed on Si surfaces at the cracks. The origin of capacity fade in the nano-dimensional multilayers is commonly related to the continuous formation of the SEI caused by the anode fracturing and pulverisation. The formation of uniform blocks with stable SEI could alleviate the problem and simultaneously promote the diffusion of Li ions along both perpendicular as well as parallel to the Si–C interfaces directions. Several disadvantages have been envisaged in the application of the ultrathin C/Si composite anodes—namely, the inherently weak mechanical strength and low initial Coulombic efficiency (CE). Despite the impressive performances, with specific capacities values above  $2500 \text{ mAh g}^{-1}$ , the proposed complex multistep fabrication procedures have hindered the commercial scale-up of multilayered C/Si anodes.

The use of C/Si composites expectantly delivers only a fraction of the nominal anode capacity compared to pure Si anodes. Nevertheless, in practical terms, such composite anodes offer advantages including faster reaction kinetics and better capacity retention. As a result, the development of commercially feasible composite anodes has been a focus for many research groups and battery manufacturers. Currently, the EU policy aimed at establishing LIB manufacturing capacity in Europe in near terms is centred on *Generation 3b* batteries and beyond, combining C/Si anodes with stable high-energy cathodes [26]. The US Advanced Battery Consortium (USABC) has set a current target for useable specific energy at  $350 \text{ Wh kg}^{-1}$  at the cell level, with further improvement to  $500 \text{ Wh kg}^{-1}$  for the next generation of batteries until 2035 [27]. Several models have shown that this target is feasible using anodes with specific capacity on the order of  $1000 \text{ mAh g}^{-1}$ . These models envisaged NMC111 as a cathode material. The specific mass (QM) of the commercial Sony 18650G8 cell— $130 \text{ mAh g}^{-1}$ —was used to account for the cell's non-active materials (electrolyte, binder, separator, current collectors, case, etc.) [28–31]. Importantly, it was

revealed that in this scenario, anode specific capacities above  $1000 \text{ mAh g}^{-1}$  would not lead to a meaningful improvement in total cell capacity.

Herein, we propose a commercially feasible, mechanically robust, high capacity, and binder-free layered carbon-silicon anode for Li-ion batteries (CALIB/Si) capable of satisfying the requirements described in the paragraph above. The CALIB/Si composite anodes were produced using the commercially scalable Virtual Cathode Deposition (VCD) [32] technique. The electrodes were formed by sequential deposition of the recently developed high-capacity carbon polymorph (CALIB) [33] coatings with  $\sim 50 \text{ nm}$ -thick Si coatings in a multilayered architecture. The VCD process enables *in situ* co-deposition from multiple targets with high rate, allowing for precise compositional and nano-dimensional control.

## 2. Materials and Methods

The anodes were produced by Virtual Cathode Deposition (VCD) on carbon veil paper (tfp-Optimat— $34 \text{ g m}^{-2}$ , Technical Fibre Products Ltd., Burneside Mills, UK). Pure carbon coatings (CALIB) and layered composites coatings (CALIB/Si) were deposited using pulsed electron beam “ablation” from two separate targets with two VCD sources—graphite (target 1) and Si (target 2)—as shown in Figure 1a. Virtual Cathode Deposition is technique that utilizes a virtual plasma cathode as a pulsed electron beam source. Prior to each pulse of the electron beam, a new plasma cathode is generated by a  $100 \text{ ns}$ ,  $10 \text{ kV}$  pulse that ionizes the operational gas. The plasma cathode acquires a negative high voltage potential relative to the target due to the application to the plasma of the high-voltage pulse. This causes pulsed electron beam extraction from the plasma boundary towards the target. The electron beam ablates the target and then the plasma cathode decays, creating space for the ablated target material, in the form of plasma plume, to propagate towards the substrate, where it condenses to form a coating. Repetition of the pulse allows the film to grow on the substrate at a controlled rate. In this work, battery anode coatings ( $\sim 2.5\text{--}3.0 \mu\text{m}$  thick) were deposited onto carbon veil paper in four different architectures (see Figure 1b):

- pure CALIB electrode acting as a reference material;
- CALIB/Si<sub>4</sub> electrode with four equally distanced  $50 \text{ nm}$ -thick Si layers;
- CALIB/Si<sub>25</sub> electrode with 25 equally distanced  $50 \text{ nm}$ -thick Si layers;
- CALIB/Si<sub>distributed</sub> electrode with silicon uniformly distributed throughout the anode thickness (the same number of pulses as in CALIB/Si<sub>4</sub>).

High-energy ions generated during VCD pulsed electron ablation have the ability to sub-plant ablated species inside the substrate or previously deposited layers, resulting in film growth from the inside out. This process induces periodic internal stress and relaxation, leading to deposition of predominantly amorphous layers interspersed with nano-crystalline clusters. A more detailed description of the method and the growth model of CALIB carbon has been published elsewhere [33,34].

The thickness of C and Si layers were controlled by sequencing the number of pulses in different ratios. The total amount of Si in the carbon matrix was estimated to  $\sim 9 \text{ wt.\%}$  (for CALIB-C/Si<sub>4</sub> and CALIB-C/Si<sub>distributed</sub>) and  $\sim 53\%$  (for CALIB-C/Si<sub>25</sub>), based on calibrated deposition rates from each target. Circular anode disks (14 mm diameter) were cut and sealed in 2032 coin half-cells using Li metal discs as counter-electrodes, Celgard separators (Celgard, LLC, Charlotte, NC, USA 28273), and  $1.0 \text{ M LiPF}_6$  in EC/DMC electrolyte. The procedure was carried out in an argon-filled glove box ( $\text{O}_2$  and water under  $1 \text{ ppm}$ ). Charge/discharge cycling tests of all cells were performed using Bio Logic tester within a voltage range  $0.1\text{--}3.0 \text{ V}$ .

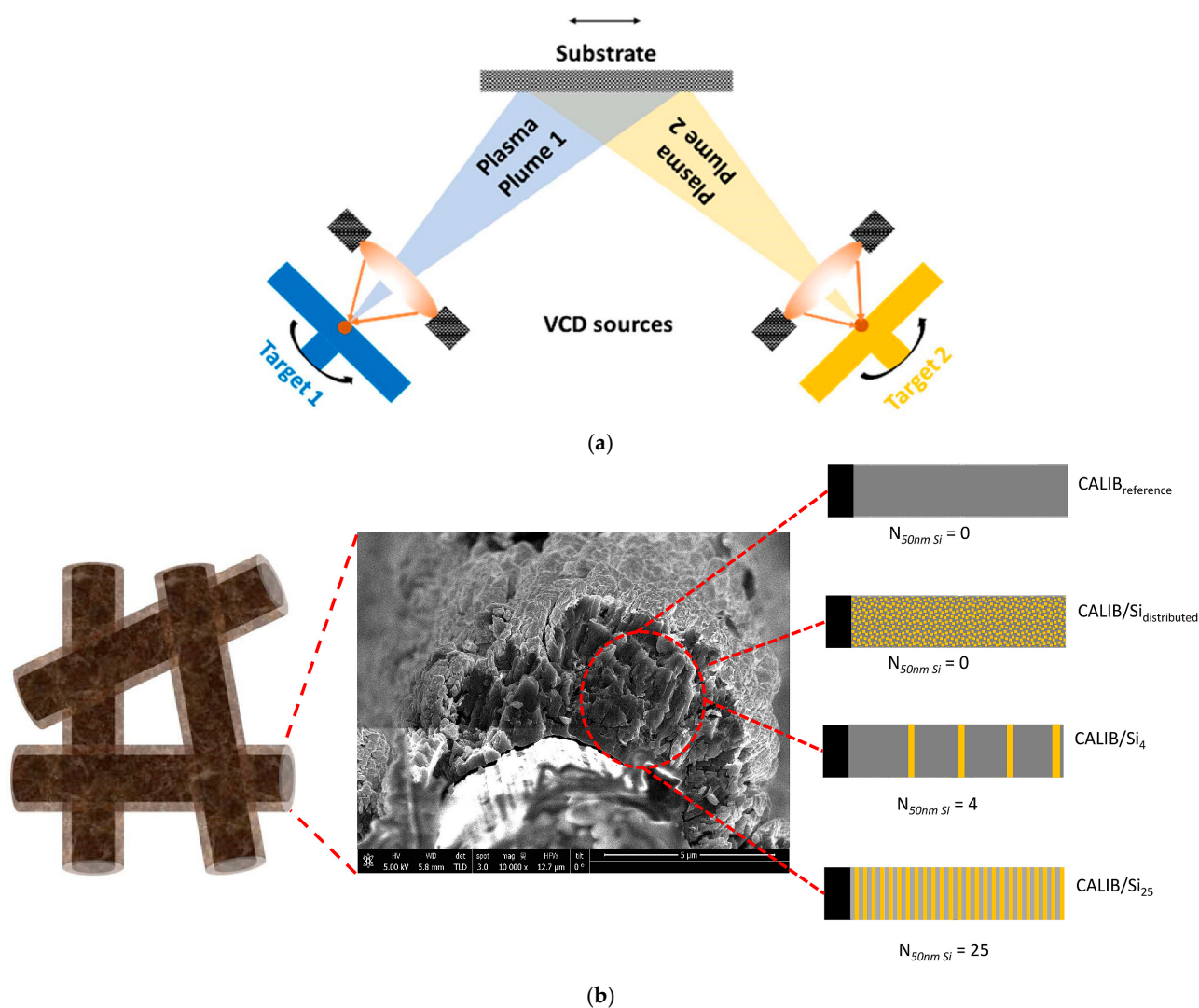


**Figure 1.** (a) Schematics of the pulsed e-beam VCD system. The plasma plumes ablated from the target is deposited on the substrate situated at distances of ~10 cm from the target; (b) schematic representation of the four different anode architectures deposited on carbon veil paper.

The properties of pure CALIB and CALIB-C/Si coatings were studied with high-resolution Scanning Electron Microscopy (HR-SEM) and Scanning Transmission Electron Microscopy (STEM—FEI Tecnai Osiris)—(Thermo Fisher Scientific Inc., Waltham, MA, USA), configured with Energy Dispersive X-ray and Electron Energy Loss Spectroscopies (EDX and EELS). Transmission Electron Microscopy (TEM), equipped with a Gatan UltraScan1000XP (2048 by 2048 pixel) camera (Gatan, Inc., Pleasanton, CA, USA) was used for high-resolution imaging. The state of disorder and bonding characteristics were analysed using Raman spectroscopy (Renishaw Ramascope-1000 instrument (514.5 nm Ar excitation laser)) (Renishaw plc, New Mills, Wotton-under-Edge, Gloucestershire, UK) operated with a holographic Notch-filter with cut-off at  $\sim 150 \text{ cm}^{-1}$ . Structural properties of CALIB and CALIB/Si coatings were characterised by X-ray diffraction (XRD) in grazing incidence (GI) and wide-angle (WA) configurations using D8 Advance Bruker diffractometers (Bruker Scientific Instruments, Billerica, MA, USA). Long counts collection times were used in order to achieve reasonable peak intensities.

### 3. Results

#### 3.1. Carbon (CALIB) Layers

High-resolution SEM images of CALIB anodes deposited on carbon veil are presented in Figure 2a,b. The cross-sectional image on Figure 2a reveal two clearly distinguishable growth zones. The zone adjacent to the substrate/layer interface (below the dotted line), is dense, with a thickness of approximately few hundred nanometres. This zone was formed during the initial stage of the growth, where the energetic carbon plume impinged directly onto the substrate interface. The second one consists of conically shaped pillars with characteristic lengths of  $\sim 0.5\text{--}1.0\ \mu\text{m}$ . The cones appear to be decorated with spiralling beads of speckle-like formations, as seen in Figure 2b. The pillars formations are compacted into an apparent porous structure with predominant mesoporosity and a large cumulative surface area of  $\sim 2000\ \text{m}^2\ \text{g}^{-1}$  [33]. Graphene sheets “veil”-type formations are present on the surfaces of the pillars as well as within the cavities of the macro pores (Figure 3a). High-resolution TEM imaging (Figure 3b) suggests that the CALIB coating consists of an amorphous carbon matrix embedded with graphitic clusters ( $\sim 20$  graphene sheets). The estimated interlayer distances ( $d_{(002)} = 0.34\text{--}0.35\ \text{nm}$ ) were elucidated to be larger than the interlayer spacing of graphite— $d_{(002)} = 0.335\ \text{nm}$  [33].

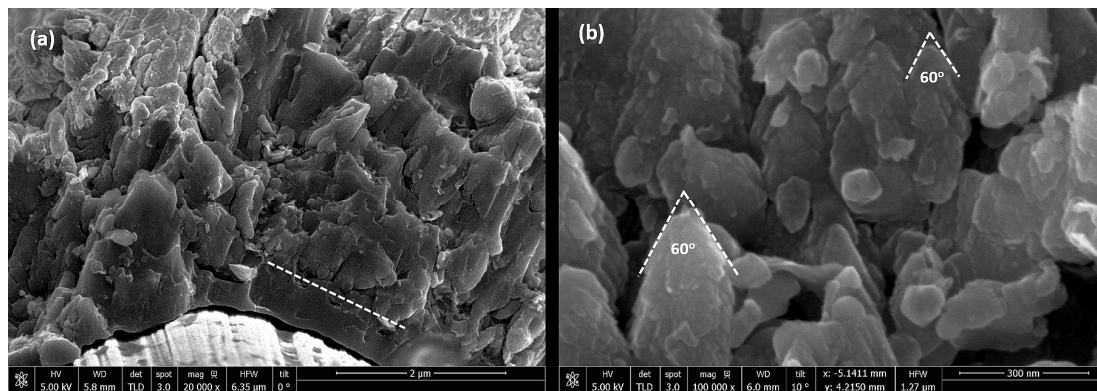


**Figure 2.** SEM images of CALIB-C coatings-deposited carbon veil substrate: (a) 20,000 $\times$  magnification and (b) 100,000 $\times$  magnification.

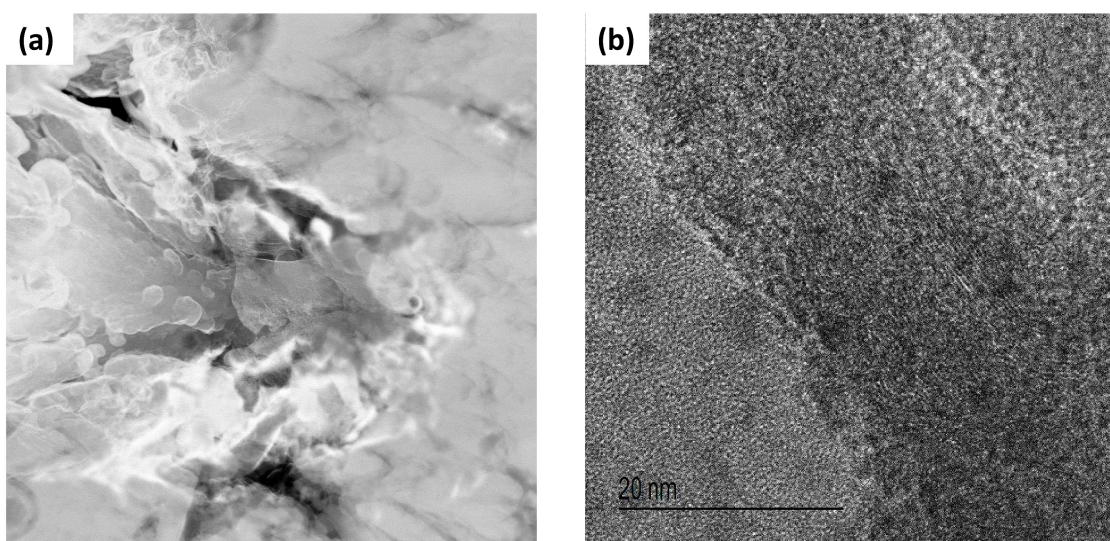


**Figure 3.** STEM images of CALIB-C coating presenting (a) graphene sheets in the inter-granular spaces and (b) graphitic clusters imbedded in amorphous matrix.

A detailed structural analysis by XPS and EELS performed, previously by D. Yarmolich et al. [33], confirmed that the bulk of the CALIB carbon coating deposited on copper foil was predominantly  $sp^2$ -bonded, with  $sp^3/sp^2$  ratio gradually increasing towards the surface. A similar  $sp^3/sp^2$  ratio bonding profile was reported in the DLC films deposited via laser ablation by E. Riedo et al. [35]. The observed microstructure and bonding state evolution conform to the well-known model of sub-plantation growth publicised by Y. Lifshitz et al. [36,37]. In the initial stage of the process, the energetic carbon species flux penetrates into the substrate, forming a dense intermixed layer with a high density of  $sp^3$ -rich zone. Subsequent pulsed energetic bombardment introduces localised periodic stress accumulation and relaxation through volume change.

The process, in turn, leads to an energetically favourable transition from  $sp^3$  to  $sp^2$  bonding and formation of an amorphous porous carbon matrix. The re-hybridisation process causes distributed formation of folded graphitic clusters, as seen in Figure 3b. We speculate that these formations serve as nucleation centres for the growth of the conical pillars. Due to the crystal symmetry of the graphene layers, the folding angle of the resulting structure can only assume multiples of 30 degrees [38]. This is experimentally evidenced by the consistent apex angle of 60 degrees observed in Figure 2b. The characteristic surface of CALIB pillars can be reasonably reconciled with the model proposed by Dong et al. [39], which describes a catalyst-free growth process of carbon whiskers with carbon layers growing perpendicular to the whisker axis in a spiral structure. The growth axis of the conical pillars is oriented along the direction of the plasma plume. Due to the energetic nature of the arriving carbon species, re-sputtering occurs, leading to substantial lateral growth and resulting in a pillar aspect ratio from ~3 to 4. The pulsed nature of carbon species super saturation around the circumference of the growing pillars leads to the formation of speckle-like beads on the surface of the cones, with an average size of ~50 nm. The as-described macro structure can be considered advantageous for the intercalation of  $Li^+$  ions intercalation, ensuring a high active surface area and opening a network of diffusion paths.

### 3.2. Composite CALIB/Si Layers

The XRD pattern of CALIB/Si<sub>4</sub> coating deposited on Cu foil was dominated by Cu substrate peaks (see Figure S1). The broad peak present between 20 and 30° was attributed to disordered bulk carbon and had previously been reported in pure CALIB coatings of varying thicknesses deposited on different substrates [33]. Notably, no reflection characteristic of crystalline Si or carbon phases were resolved, suggesting that Si interlayer growth conformed to the CALIB carbon matrix. GI-XRD of the pure CALIB coating (~4 μm thick), presented as an inset in Figure S1, further illustrates the disordered nature of the VCD-deposited carbon layer. The possible presence of nano crystallites could not be confirmed using XRD due to the fluctuating distribution of the nanosized clusters [40] and the likely adsorption of water molecules during sample handling in open air [41].

Figures 4a,c and S2 present TEM cross-sectional views of FIB milled CALIB-C/Si<sub>4</sub> coating deposited on Cu substrate. The layered distribution of Si throughout C/Si electrode is clearly visible in the EDX elemental mapping shown in Figure 4b. The EDX mapping shows four well-defined, uniformly spaced Si layers (approximately 50 nm thick), each separated by ~500 nm of carbon. The interface between the carbon and silicon layers in CALIB-C/Si<sub>4</sub> sample was observed to be coherent and defect-free, with a small degree of carbon–silicon intermixing. Importantly, the Si layers are embedded within the CALIB matrix without disrupting the CALIB pillar-type structure, suggesting similarity in the growth modes of both carbon and silicon. A comparison of the microstructure and the low-loss EELS spectra recorded in the regions of the silicon layer and the carbon matrix can be seen in

Figure 4c,d. The peaks in the low-loss EELS spectra appearing at 16.7 eV and 33.4 eV have previously been reported as bulk plasmon losses of c-Si [42,43]. The plasmon peak at  $\sim$ 26 eV in the carbon matrix spectrum is conventionally assigned to amorphous carbons. SEM and EDX map cross-sectional images for CALIB-C/Si<sub>4</sub> (Figure S3a,b) and CALIB-C/Si<sub>distributed</sub> anodes (Figure S3c,d) demonstrate the coherent Si distribution within the CALIB matrix.

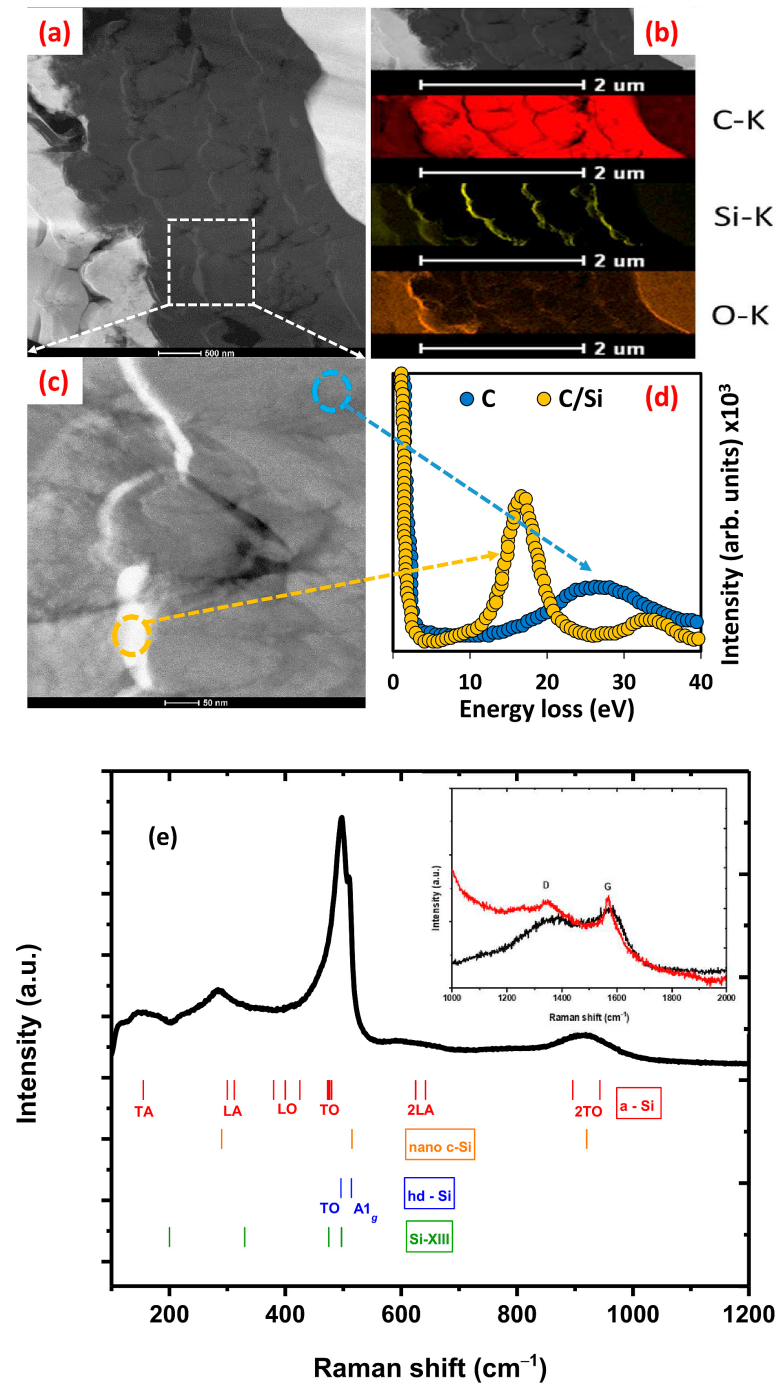


**Figure 4.** (a) TEM cross-section image of C/Si coating and the area within which EELS spectra were recorded; (b) EDX mapping of C, Si and O superimposed to the relevant slice of the image; (c) expanded image of a Si layer following the shape of the pillar; (d) EELS spectra of the Si layer (orange) and carbon matrix (blue) areas; (e) Raman spectra of the CALIB/Si<sub>25</sub> superimposed to the positions of the Raman peaks reported for metastable Si phases (see Table 1 and the references therein). (The inset in Figure 4e shows a comparison of Raman spectra of CALIB/Si<sub>25</sub> and CALIB coatings in the range of 1000 to 2000 cm<sup>-1</sup>).

To evaluate the short- and mid-range order of the composite material, Raman spectra were acquired from both CALIB-C/Si<sub>25</sub> and CALIB-C coatings. The Raman spectrum of CALIB-C/Si<sub>25</sub>, shown in Figure 4e, reveals a multi-band profile with a notable absence of a peak at 520 cm<sup>-1</sup>, which conventionally arises from crystalline Si. This absence indicates the lack of standard diamond cubic structure (dc-Si). Characteristic peaks positions previously associated by various authors with amorphous Si are indicated in red below the spectrum. Four distinct phonon bands observed at wavenumbers below 480 cm<sup>-1</sup> (transverse acoustic (TA) at 146 cm<sup>-1</sup>, longitudinal acoustic (LA) at 285 cm<sup>-1</sup>, longitudinal optic (LO) at 399 cm<sup>-1</sup>, and transverse optic (TO) at 470 cm<sup>-1</sup>) are typically associated with the presence of amorphous Si vibrational modes [44–48]. Raman spectra of nanocrystalline Si have previously been reported to exhibit a strong peak at 515 cm<sup>-1</sup>, along with a weaker bands at ~290 cm<sup>-1</sup> and ~920 cm<sup>-1</sup>, corresponding to the Si–Si stretching vibration mode of the crystalline dc-Si phase [49]. The broad features with lower intensity, positioned at ~660 cm<sup>-1</sup> and ~910 cm<sup>-1</sup>, are sometimes attributed to the second-order phonon modes (denoted as 2LA and 2TO) of a-Si. However, some authors argue that the broad feature between 630 and 670 cm<sup>-1</sup> may be a superposition of modes characteristic of nano-crystalline dc-Si, which can be ascribed to a quantum confinement effect [50,51]. The major band appearing in the range of 480–510 cm<sup>-1</sup> suggests the presence of a nano crystalline component distributed within the amorphous Si matrix, thereby emulating the structural characteristics of the CALIB material. It is difficult to reliably assign the 480–510 cm<sup>-1</sup> band to nano dc-Si phase by referencing the CALIB-C/Si<sub>25</sub> spectra to previously reported Raman peaks. Raman bands of two different metastable phases—hd-Si and Si-XIII—can also be considered. The position of the Raman peaks related to a-Si, nano dc-Si, hd-Si, and Si-XIII are marked in Figure 4e. Exotic phases like hd-Si (hexagonal diamond structure, P6<sub>3</sub>/mmc space group) and Si-XIII (structural data not available) are typically formed through annealing of the metastable bc8/r8-Si phase. The latter has been experimentally obtained under high-pressure conditions, including diamond anvil cell, femtosecond laser irradiation, and uniaxial point loading via indentation [52]. Raman peaks associated with Si-XIII phase have also been reported alongside those of the hd-Si phase in the transformation pathway -(r8-Si → bc8-Si → hd-Si/Si-XIII → dc-Si) as described by Domnich et al. [53]. The authors observed also a direct transition from the hd-Si/Si-XIII phase to the a-Si phase, which could explain the coexistence of both amorphous and nano-crystalline phases. Due to the significant overlap in the Raman bands and the uncertainty of Raman modes positions—which depend on the degree of amorphisation—it is difficult to confidently assign the nano-crystalline fraction in the VCD-deposited silicon to nano dc-Si phase. One must account for the high-energy nature of the VCD (PED) method, which could conceivably produce a metastable Si phase. The Raman spectra of CALIB-C/Si<sub>25</sub> coating at higher wavenumbers revealed the presence of the D and G broad peaks typical of the CALIB electrode (see the inset in Figure 4e). The G-band corresponds to the stretching vibration mode of graphite, while the D-band reflects disorder in the carbon matrix. Notably, the positions of the D and G bands are similar in both electrodes. The integrated intensity ratio R ( $I_D/I_G$ ) for both CALIB and CALIB-C/Si<sub>25</sub> was evaluated to be ~0.9–1.0, indicating a high degree of disorder.

The Raman and the reference data reported in [54–57] are summarised in Table 1, suggesting that the Si multilayers in the electrodes preserve the disordered microstructure of the CALIB material, with some detectable amounts of nanocrystalline phases embedded in the amorphous Si matrix.

**Table 1.** The Raman peaks associated with different experimentally observed phases of Si compared to the Raman peaks of CALIB-C/Si<sub>25</sub> coating. Relevant references shown at the bottom of each column.

dc-Si	a-Si	hd-Si	Si-XIII	CALIB-C/Si <sub>25</sub>
Raman shift, cm <sup>-1</sup>				
290 (TA)	155 (TA)	496 (TO)	200	146
515 (TO)	300 (LA)	514 (A1 <sub>g</sub> )	330	284
920 (2TO)	312 (LA)		475	400
	380 (LO)		497	463
	400 (LO)			488
	425 (LO)			498
	473 (TO)			665
	475 (TO)			912
	477 (TO)			
	480 (TO)			
	625 (2LA)			
	642 (2LA)			
	896 (2TO)			
	943 (2TO)			
Refs. [48–50]		Refs. [43–47]		Refs. [51,53]
		Refs. [51,53]		Refs. [51–54]

### 3.3. Electrochemical Characterisation

The initial specific capacities of the anodes were measured in half-cell configuration (vs. Li/Li<sup>+</sup>) at a current rate of 0.1 A/g. Figure 5a compares the first and fourth charge/discharge cycles of CALIB/Si<sub>4</sub> and reference CALIB electrodes. The pure carbon electrode exhibited a first cycle capacity of approximately 1200 mAh g<sup>-1</sup>, which decreases to ~960 mAh g<sup>-1</sup> by the fourth cycle. The CALIB-C/Si<sub>4</sub> composite electrodes showed a substantially higher first-cycle discharge specific capacity of approximately 2100 mAh g<sup>-1</sup>, decreasing to about 1500 mAh g<sup>-1</sup> in the fourth cycle. The first-cycle irreversibilities for both the CALIB-C/Si<sub>4</sub> and CALIB electrodes were found to be ~20%. Normalised differential capacity curves of the first and the second cycles for CALIB and CALIB-C/Si<sub>4</sub> vs. Li/Li<sup>+</sup> are superimposed in Figure 5b. Compared to CALIB electrode, the CALIB-C/Si<sub>4</sub> electrode exhibits two additional distinctive peaks in the lithiation curve and two peaks in the delithiation curve. The peaks at ~0.17–0.20 and ~0.05 V are attributed to intermediate lithiation stoichiometry of Li<sub>2.2</sub>Si and Li<sub>3.5</sub>Si [58]. The peak at 0.33 V is ascribed to the delithiation of the amorphous phase, while the second peak at ~0.45 V is assigned to the delithiation of the crystalline phase [59]. The appearance of a small broad peak at ~1.7 V is attributed to the formation of SEI film. Additionally, the broad band of small anodic peaks between 0.11 and 0.25 V is associated with the graphitic component.

CALIB-C/Si<sub>4</sub> and CALIB electrodes exhibit good cycling performance at higher current rate of 1 A g<sup>-1</sup> for 200 cycles, as illustrated in Figure 5c. After an initial rapid capacity fade, the discharge curve stabilizes, resulting in a limited loss of approximately 0.1–0.2% per cycle. Specific capacities of ~720 mAh g<sup>-1</sup> for CALIB and ~1080 mAh g<sup>-1</sup> for CALIB-C/Si<sub>4</sub> were recorded at cycle 200 with ~99% Coulombic efficiency for both electrodes. The typical rate performance of a CALIB-C/Si<sub>4</sub> electrode at 0.1 A/g, 1 A/g and 2 A/g during sequential discharge cycling is presented in Figure S5. The good capacity retention in CALIB-C/Si<sub>4</sub> is attributed to the presence of mesoporous carbon matrix, which efficiently accommodates the stress caused by the alloying/de-alloying of silicon nano-layers. This buffers the pulverisation effect and preserves the structural integrity of the composite. The layered architecture of the electrode results in the carbon matrix dominating the irreversibility behaviour of the C/Si anode due to its much larger active surface area.

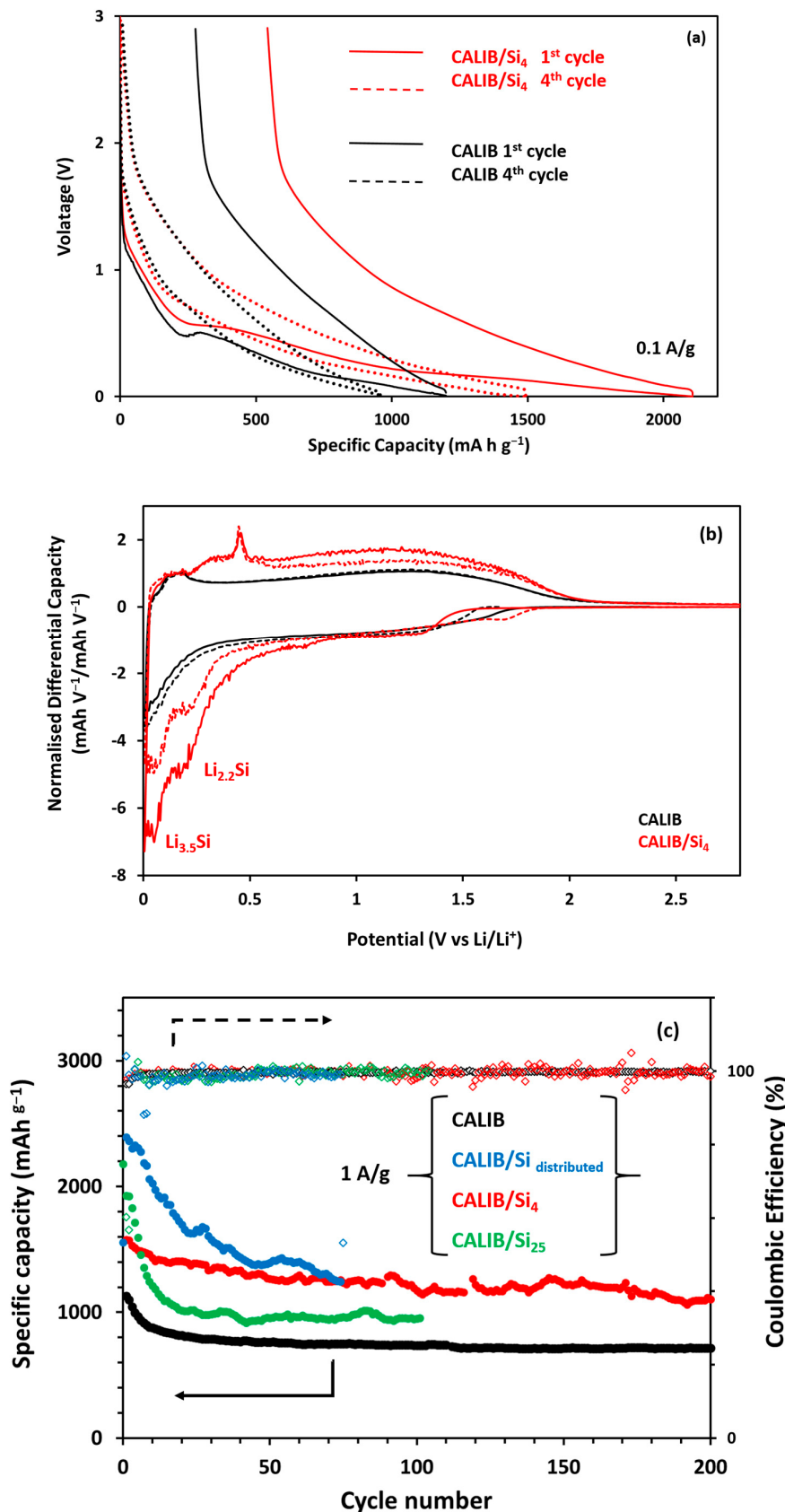


**Figure 5.** (a) First 4 cycles of discharge/charge of CALIB-C and CALIB-C/Si<sub>4</sub> at a  $0.1 \text{ A.g}^{-1}$  rate; (b) comparative analysis of the 1st and the 2nd cycle total differential capacity plots for CALIB and CALIB-C/Si<sub>4</sub> electrodes ( $dQ/dV$  curves normalised to that of a pure graphite electrode); (c) extended cycling (100 cycles) of all three anodes at  $1 \text{ A.g}^{-1}$  rate. All cells cycled vs. Li/Li<sup>+</sup> in 1.0 M LiPF<sub>6</sub> in EC/DMC electrolyte.

Such losses are considered to be caused by (i) the formation of a solid electrolyte interphase (SEI) film over the large surface area, which irreversibly consumes lithium inventory, and (ii) the reaction of Li ions with surface functional groups covalently bonded to the edges of hexagonal carbon fragments during air exposure of the electrode [60,61]. As demonstrated in our previous work [33], the irreversible capacity can be reduced by growing thicker CALIB coatings. However, this approach is impractical, as it leads to deterioration of the carbon and silicon target surfaces. Further attempts to reduce the irreversible losses involved depositing CALIB coatings directly onto a ceramic-coated separator, followed by the in situ deposition of a sealing copper thin layer. This approach appeared to reduce the electrode's sensitivity to air exposure and led to a substantial decrease in irreversible losses (~9%). A schematic illustration of the result is shown in Figure S4. A more detailed description of the experiment can be found in reference [33].

A sharper capacity decline was recorded for the CALIB-C/Si<sub>25</sub> anode during the first ~20 cycles, followed by a gradual decay that reached a specific capacity of ~950 mAh g<sup>-1</sup> at cycle 100. Overall, the performance of CALIB-C/Si<sub>25</sub> electrode at high current rates appeared inferior, which could be attributed to (i) less efficient buffering by the thinner CALIB interlayers; (ii) narrower pathways for Li ions diffusion parallel to the Si/C interfaces; and (iii) continuous re-formation of SEI along the Si/C interface. The initial specific capacity of CALIB-C/Si<sub>distributed</sub> electrode was higher, at ~2400 mAh g<sup>-1</sup>. However, the cycling run lead to a faster decline in the performance, with the cell failing at cycle number 75.

To assess the effects of gradual pulverisation and SEI reformation, cross-sectional images of CALIBC/Si<sub>25</sub> electrode were taken before cycling (pristine electrode—Figure 6a,b) and after the long-term cycling (post-mortem—Figure 6c,d). There is a lack of evidence of catastrophic macroscopic cracking in the Si layers within the pillars, which supports the observed long-term cycling stability. While SEI formation is primarily concentrated at the borders of the pillars, some SEI can also be detected in defect-rich regions along the CALIB/Si interface. The latter loss of Li inventory is accounting for the initial accelerated capacity loss in the CALIB-C/Si<sub>25</sub> anode. We speculate that the reduced capacity of CALIB-C/Si<sub>25</sub> is mainly due to obstructed Li<sup>+</sup> ion transport along the C/Si interface, which renders portions of the silicon material electrochemically inactive.

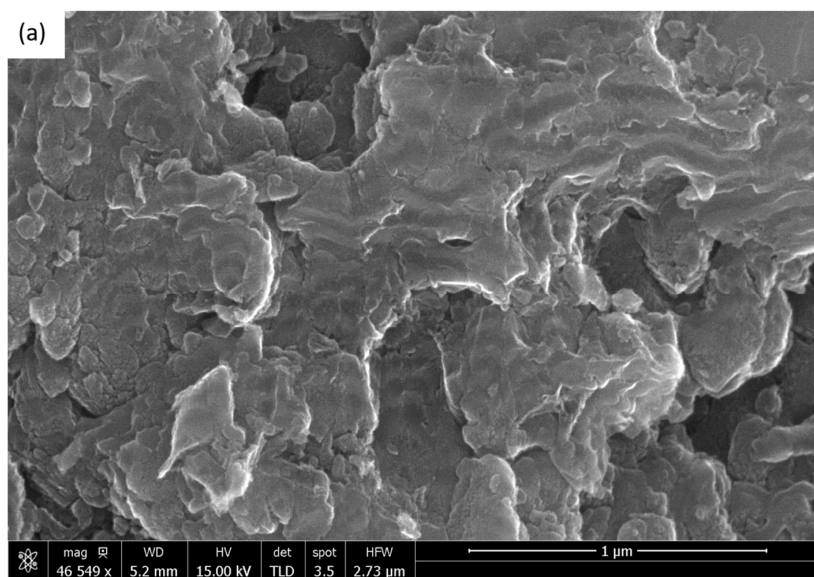


**Figure 6. Cont.**

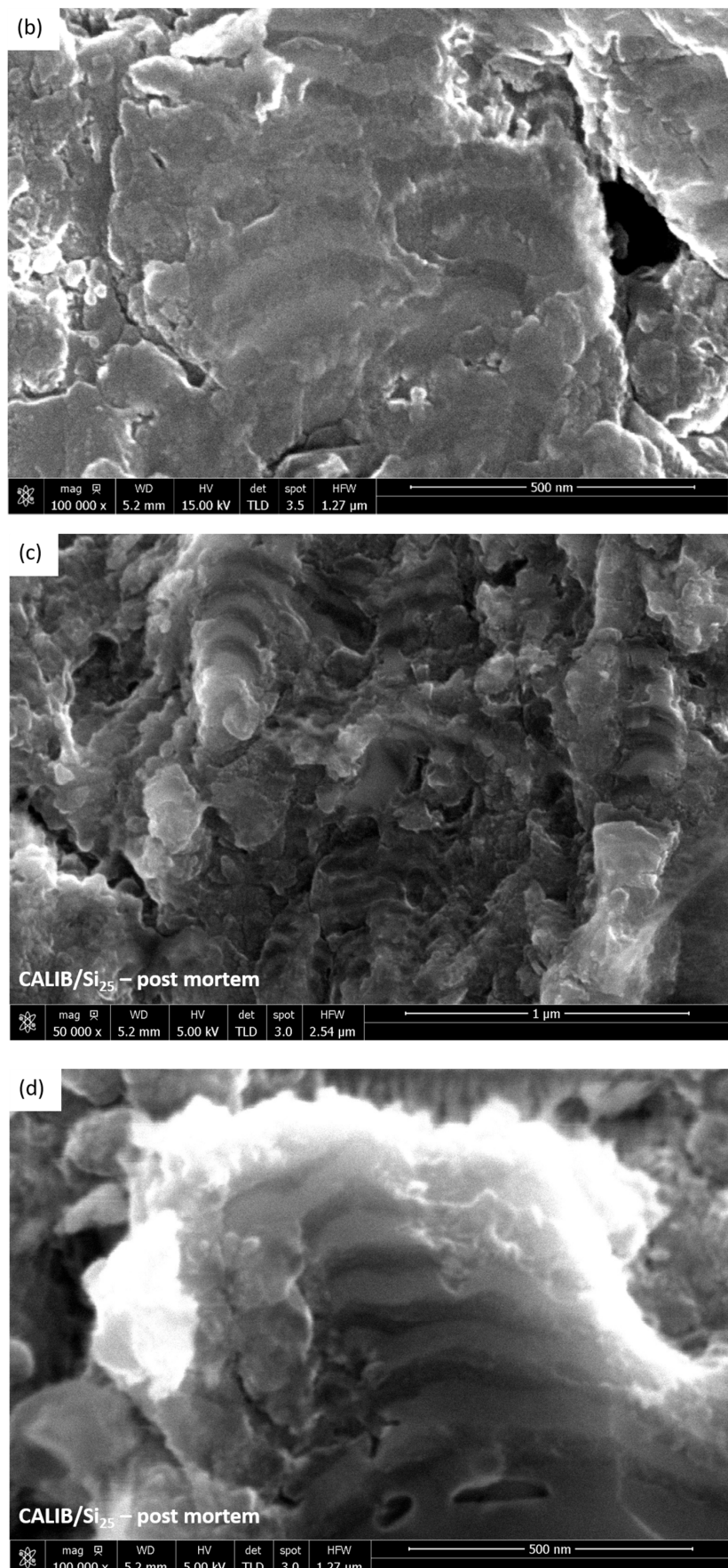


Figure 6. HR-SEM cross-sectional images of pristine (a,b) and post-mortem (c,d) CALIB-C/Si<sub>25</sub> electrodes.

#### 4. Conclusions

The reported results demonstrate the feasibility of CALIB-C/Si<sub>n</sub> anodes with high gravimetric capacities. A substantial increase in gravimetric density over commercial graphite anodes was achieved using scalable VCD technology, capable of depositing large-area coatings at a kHz pulse rate. The binder-free electrodes, along with the ability to deposit CALIB-C/Si<sub>n</sub> multilayers on various substrates, enable the development of composite anodes for various applications.

The silicon layers were found to consist of an amorphous Si matrix with embedded nanocrystalline components, emulating the growth mode of the CALIB layer, which comprised a disordered carbon matrix encompassing nanosized sp<sup>2</sup>-bonded graphitic clusters cross-linked by a network of sp<sup>3</sup>-bonded atomic sites [33]. The presence of the mesoporous carbon matrix accommodates the stress caused by the alloying/de-alloying of silicon nanolayers, thereby alleviating the pulverisation effect and preserving the structural integrity of the composite.

The initial performance and capacity decay of the anodes were found to depend on the thickness of the CALIB buffer interlayers. Charge/discharge cycling at a current rate of 1 A g<sup>-1</sup> revealed that the incorporation of ~9 wt.% Si into the CALIB matrix contributed to a ~50% enhancement in anode-specific capacity, reaching ~1080 mAh g<sup>-1</sup> after 200 cycles. Irreversibility and capacity retention are primarily influenced by the characteristics and thickness of the CALIB buffer layers.

Increasing the Si content above 50 wt.% did not lead to a proportional capacity increase due to the insufficient buffering effect of the thinner CALIB interlayers and the hindrance of Li<sup>+</sup> ion diffusion. Modifying the electrode architecture by optimising the number of nano-Si layers and their separation distance is expected to further improve the performance of the composite layered nano C/Si anode.

VCD-CALIB technology presents a feasible path toward the commercialisation of nano-engineered composite battery electrodes. We estimate the current development of the VCD (PED) method to be at Technological Readiness Level (TRL) 5. The method is universal in its ability to ablate and deposit various types of dissimilar materials while preserving the stoichiometry of multi-component targets in the resulting coatings. VCD (PED) can fabricate *in situ* multilayered architectures through the simultaneous use of several VCD sources, enabling the deposition of anode layers, separators (e.g., ceramics), and complex cathode compositions.

Scaling the deposition of CALIB coatings over an area of 10 × 10 cm<sup>2</sup> has already been demonstrated on a scanning Cu foil substrate [33]. To adapt the technology for industrial roll-to-roll processes, achieving low operational expenditure (OPEX) is essential. A major obstacle to this goal is the rapid erosion of expensive ultra-pure targets during extended operation, as well as the high cost of vacuum equipment.

Therefore, we envisage initial commercial applications in the high-value, high-performance, all-solid-state “battery on demand” market.

**Supplementary Materials:** The following supporting information can be downloaded at: <https://www.mdpi.com/article/10.3390/batteries1110400/s1>, Figure S1. WA-XRD spectra of CALIB/Si<sub>4</sub> coating deposited on Cu substrate. The inset shows GI-XRD spectra of 4 μm thick pure CALIB coating; WA-XRD spectrum of CALIB/Si<sub>4</sub> coating was scanned with step size of 0.02°/step. Figure S2. TEM cross-section image of CALIB/Si<sub>4</sub> coating illustrating the interface between Si layer and CALIB buffer and their characteristic thicknesses. Figure S3. SEM and EDX map representations of cross-sections for CALIB-C/Si<sub>4</sub> (a and b) and CALIB-C/Si<sub>distributed</sub> (c and d) anodes. Figure S4. The first discharge/charge cycle of an CALIB coating deposited directly onto the ceramic-coated separator followed by *in-situ* deposition of sealing layer of copper)—see reference [33]. Figure S5. Rate performance of a CALIB-C/Si<sub>4</sub> electrode at 0.1 A/g, 1 A/g and 2 A/g in sequential discharge cycling.

**Author Contributions:** Conceptualisation, R.I.T., D.Y. and V.K.; methodology, R.I.T. and D.Y.; investigation, R.I.T. and D.Y.; writing—original draft, R.I.T.; writing—review and editing, D.Y. and V.K.; supervision, V.K. All authors have read and agreed to the published version of the manuscript.

**Funding:** This work was supported by UK IAA Project number RG90413/20116.

**Data Availability Statement:** The original contributions presented in this study are included in the article/Supplementary Materials. Further inquiries can be directed to the corresponding author.

**Conflicts of Interest:** Author Dmitry Yarmolich was employed by the company Plasma App Ltd. The remaining authors declare that the research was conducted in the absence of any commercial or financial relationships that could be construed as a potential conflict of interest.

## References

1. Dunn, B.; Kamath, H.; Tarascon, J.M. Electrical energy storage for the grid: A battery of choices. *Science* **2011**, *334*, 928–935. [[CrossRef](#)] [[PubMed](#)]
2. Cano, Z.P.; Ye, S.; Hintennach, A.; Lu, J.; Fowler, M.; Chen, Z. Batteries and fuel cells for emerging electric vehicle markets. *Nat. Energy* **2018**, *3*, 279–289. [[CrossRef](#)]
3. Khomenko, V.G.; Barsukov, V.Z. Characterization of silicon- and carbon-based composite anodes for lithium-ion batteries. *Electrochim. Acta* **2007**, *52*, 2829–2840. [[CrossRef](#)]
4. Dahn, J.R.; Zheng, T.; Liu, Y.H.; Xue, J.S. Mechanisms for Lithium Insertion in Carbonaceous Materials. *Science* **1995**, *270*, 590–593. [[CrossRef](#)]
5. Jin, B.; Liao, L.; Shen, X.; Mei, Z.; Du, Q.; Liang, L.; Lei, B.; Du, J. Advancement in Research on Silicon/Carbon Composite Anode Materials for Lithium-Ion Batteries. *Metals* **2025**, *15*, 386. [[CrossRef](#)]
6. Feyzi, E.; Anil Kumar, M.R.; Li, X.; Deng, S.; Nanda, J.; Zaghib, K. A comprehensive review of silicon anodes for high-energy lithium-ion batteries: Challenges, latest developments, and perspectives. *Next Energy* **2024**, *5*, 100176. [[CrossRef](#)]
7. Yang, Y.; Dong, R.; Cheng, H.; Wang, L.; Tu, J.; Zhang, S.; Zhao, S.; Zhang, B.; Pan, H.; Lu, Y. 2D Layered Materials for Fast-Charging Lithium-Ion Battery Anodes. *Small* **2023**, *19*, e2301574. [[CrossRef](#)]
8. Cai, X.; Lai, L.; Shen, Z.; Lin, J. Graphene and graphene-based composites as Li-ion battery electrode materials and their application in full cells. *J. Mater. Chem. A* **2017**, *5*, 15423–15446. [[CrossRef](#)]
9. Mi, C.H.; Cao, G.S.; Zhao, X.B. A non-GIC mechanism of lithium storage in chemical etched MWNTs. *J. Electroanal. Chem.* **2004**, *562*, 217–221. [[CrossRef](#)]
10. Guo, P.; Song, H.H.; Chen, X.H. Electrochemical performance of graphene nanosheets as anode material for lithium-ion batteries. *Electrochim. Commun.* **2009**, *11*, 1320–1324. [[CrossRef](#)]
11. Liu, X.H.; Zhong, L.; Huang, S.; Mao, S.X.; Zhu, T.; Huang, J.Y. Size-Dependent Fracture of Silicon Nanoparticles During Lithiation. *ACS Nano* **2012**, *6*, 1522–1531. [[CrossRef](#)] [[PubMed](#)]
12. Ahmed, H.A.; Simoes dos Reis, G.; Molaiyan, P.; Lähde, A.; Lassi, U. Silicon/carbon composite anode materials for lithium-ion batteries: Materials design and synthesis, current state, progress, and future perspectives. *Prog. Energy* **2025**, *7*, 022003. [[CrossRef](#)]
13. Shen, X.; Tian, Z.; Fan, R.; Shao, L.; Zhang, D.; Cao, G.; Kou, L.; Bai, Y. Research progress on silicon/carbon composite anode materials for lithium-ion battery. *J. Energy Chem.* **2018**, *27*, 1067–1090. [[CrossRef](#)]
14. Liu, X.; Zhu, X.; Pan, D. Solutions for the problems of silicon–carbon anode materials for lithium-ion batteries. *R. Soc. Open Sci.* **2018**, *5*, 172370. [[CrossRef](#)]
15. Kumar, S.K.; Ghosh, S.; Malladi, S.K.; Nanda, J.; Martha, S.K. Nanostructured Silicon–Carbon 3D Electrode Architectures for High-Performance Lithium-Ion Batteries. *ACS Omega* **2018**, *3*, 9598–9606. [[CrossRef](#)]
16. Chen, Y.; Hu, Y.; Shen, Z.; Chen, R.; He, X.; Zhang, X.; Zhang, Y.; Wu, K. Sandwich structure of graphene-protected silicon/carbon nanofibers for lithium-ion battery anodes. *Electrochim. Acta* **2016**, *210*, 53–60. [[CrossRef](#)]
17. Pan, Q.; Zuo, P.; Lou, S.; Mu, T.; Du, C.; Cheng, X.; Ma, Y.; Gao, Y.; Yin, G. Micro-sized spherical silicon@carbon@graphene prepared by spray drying as anode material for lithium-ion batteries. *J. Alloys Compd.* **2017**, *723*, 434–440. [[CrossRef](#)]
18. Dou, F.; Shi, L.; Chen, G.; Zhang, D. Silicon/Carbon Composite Anode Materials for Lithium-Ion Batteries. *Electrochim. Energy Rev.* **2019**, *2*, 149–198. [[CrossRef](#)]
19. An, Y.; Tian, Y.; Liu, C.; Xiong, S.; Feng, J.; Qian, Y. One-Step, Vacuum-Assisted Construction of Micrometer-Sized Nanoporous Silicon Confined by Uniform Two-Dimensional N-Doped Carbon toward Advanced Li Ion and MXene-Based Li Metal Batteries. *ACS Nano* **2022**, *16*, 4560–4577. [[CrossRef](#)]
20. An, Y.; Tian, Y.; Zhang, Y.; Wei, C.; Tan, L.; Zhang, C.; Cui, N.; Xiong, S.; Feng, J.; Qian, Y. Commercial Alloy and CO<sub>2</sub> for Lithium Storage and Flexible Ti3C<sub>2</sub>Tx MXene-Based Lithium–Metal Batteries. *ACS Nano* **2020**, *14*, 17574–17588. [[CrossRef](#)] [[PubMed](#)]

21. Li, J.; Dozier, A.K.; Li, Y.; Yang, F.; Cheng, Y.-T. Crack Pattern Formation in Thin Film Lithium-Ion Battery Electrodes. *J. Electrochem. Soc.* **2011**, *158*, A689–A694. [CrossRef]
22. Ryu, J.; Chen, T.; Bok, T.; Song, G.; Ma, J.; Hwang, C.; Luo, L.; Song, H.-K.; Cho, J.; Wang, C.; et al. Mechanical mismatch-driven rippling in carbon-coated silicon sheets for stress-resilient battery anodes. *Nat. Commun.* **2018**, *9*, 2924. [CrossRef] [PubMed]
23. Sayed, S.Y.; Kalisvaart, W.P.; Olsen, B.C.; Luber, E.J.; Xie, H.; Buriak, J.M. Alternating Silicon and Carbon Multilayer-Structured Anodes Suppress Formation of the c-Li<sub>3.75</sub>Si Phase. *Chem. Mater.* **2019**, *31*, 6578–6589. [CrossRef]
24. Zhao, Y.; Wang, J.; He, Q.; Shi, J.; Zhang, Z.; Men, X.; Yan, D.; Wang, H. Li-Ions Transport Promoting and Highly Stable Solid-Electrolyte Interface on Si in Multilayer Si/C through Thickness Control. *ACS Nano* **2019**, *13*, 5602–5610. [CrossRef]
25. Yang, L.; Chen, H.-S.; Jiang, H.Q.; Wei, Y.J.; Song, W.L.; Fang, D.N. Failure mechanisms of 2D silicon film anodes: In situ observations and simulations on crack evolution. *Chem. Commun.* **2018**, *54*, 3997–4000. [CrossRef] [PubMed]
26. Nationale Plattform Elektromobilität: Roadmap Integrierte Zell-und Batterieproduktion Deutschland, January 2016. Available online: [https://www.plattform-zukunft-mobilitaet.de/wp-content/uploads/2021/12/2016\\_Roadmap\\_integrierte\\_Zell\\_und\\_Batterieproduktion\\_Deutschland.pdf](https://www.plattform-zukunft-mobilitaet.de/wp-content/uploads/2021/12/2016_Roadmap_integrierte_Zell_und_Batterieproduktion_Deutschland.pdf) (accessed on 1 September 2025).
27. The Faraday Institution. *High-Energy Battery Technologies*; Faraday Report—2020; The Faraday Institution: Didcot, UK, 2020; Available online: <https://faraday.ac.uk/wp-content/uploads/2020/01/High-Energy-battery-technologies-FINAL.pdf> (accessed on 1 September 2025).
28. Kasavajjula, U.; Wang, C.; Appleby, A.J. Nano- and bulk-silicon-based insertion anodes for lithium-ion secondary cells. *J. Power Sources* **2017**, *163*, 1003–1039. [CrossRef]
29. Yim, C.-H.; Niketic, S.; Salem, N.; Naboka, O.; Abu-Lebdeh, Y. Towards Improving the Practical Energy Density of Li-Ion Batteries: Optimization and Evaluation of Silicon: Graphite Composites in Full Cells. *J. Electrochem. Soc.* **2017**, *164*, A6294–A6302. [CrossRef]
30. Yim, C.-H.; Courtel, F.M.; Abu-Lebdeh, Y. A high capacity silicon-graphite composite as anode for lithium-ion batteries using low content amorphous silicon and compatible binders. *J. Mater. Chem. A* **2013**, *1*, 8234–8243. [CrossRef]
31. Obrovac, M.N.; Christensen, L.; Le, D.B.; Dahn, J.R. Alloy Design for Lithium-Ion Battery Anodes. *J. Electrochem. Soc.* **2007**, *154*, A849–A855. [CrossRef]
32. Yarmolich, D. Virtual Cathode Deposition (vcd) for Thin Film Manufacturing. WO2016/042530 A1, 24 March 2016.
33. Yarmolich, D.; Odarchenko, Y.; Murphy, C.; Petrucco, E.A.; Cookson, J.; Yarmolich, D.; Zhao, T.; Kim, H.-K.; Kumar, R.V.; Tomov, R.I. Novel binder-free carbon anode for high capacity Li-ion batteries. *Nano Energy* **2021**, *83*, 105816. [CrossRef]
34. Yarmolich, D.; Vekselman, V.; Gurovich, V.T.; Felsteiner, J.; Krasik, Y.E. Energetic particle and photon emission during dense plasma formation at the ferroelectric surface. *Plasma Sources Sci. Technol.* **2008**, *17*, 35002–35011. [CrossRef]
35. Riedo, E.; Comin, F.; Chevrier, J.; Schmithusen, F.; Decossas, S.; Sancrotti, M. Structural properties and surface morphology of laser-deposited amorphous carbon and carbon nitride films. *Surf. Sci. Technol.* **2000**, *125*, 124–128. [CrossRef]
36. Lifshitz, Y.; Köhler, T.; Frauenheim, T.; Guzmann, I.; Hoffman, A.; Zhang, R.Q.; Zhou, X.T.; Lee, S.T. The Mechanism of Diamond Nucleation from Energetic Species. *Science* **2002**, *297*, 1531–1533. [CrossRef]
37. Lifshitz, Y.; Kasi, S.R.; Rabalais, J.W.; Eckstein, W. Subplantation model for film growth from hyperthermal species. *Phys. Rev. B* **1990**, *41*, 10468–10480. [CrossRef]
38. Ebbesen, T. Sheets, cones, balls and tubes. In *Carbon Molecules and Materials*; Setton, R., Bernier, P., Lefrant, S., Eds.; Taylor & Francis Group, LLC.: Abingdon, UK, 2002; pp. 181–186.
39. Dong, J.; Shen, W.; Zhang, B.; Liu, X.; Kang, F.; Gu, J.; Li, D.; Chen, N.-P. New origin of spirals and new growth process of carbon whiskers. *Carbon* **2001**, *39*, 2325–2333. [CrossRef]
40. Fujimoto, H. Theoretical X-ray scattering intensity of carbons with turbostratic stacking and AB stacking structures. *Carbon* **2003**, *41*, 1585–1592. [CrossRef]
41. Laszlo, K.; Czakkel, O.; Dobos, G.; Lodewyckx, P.; Rochas, C.; Geissler, E. Water vapour adsorption in highly porous carbons as seen by small and wide angle X-ray scattering. *Carbon* **2010**, *48*, 1038–1048. [CrossRef]
42. Wang, J.; Wang, X.F.; Li, Q.; Hryciw, A.; Meldrum, A. The microstructure of SiO thin films: From nanoclusters to nanocrystals. *Philosoph. Mag.* **2007**, *87*, 11–27. [CrossRef]
43. Available online: <https://eelsdb.eu/spectra/silicon-5/> (accessed on 15 May 2025).
44. Yang, G.; Li, X.; Cheng, Y.; Wang, M.; Ma, D.; Sokolov, A.P.; Kalinin, S.V.; Veith, G.M.; Nanda, J. Distilling nanoscale heterogeneity of amorphous silicon using tip-enhanced Raman spectroscopy (TERS) via multiresolution manifold learning. *Nat. Commun.* **2021**, *12*, 578. [CrossRef]
45. Shrestha, K.; Whitfield, D.; Lopes, V.C.; Syllaios, A.J.; Littler, C.L. Electrical Conductivity and Structural Order of p-Type Amorphous Silicon Thin Films. *Mater. Res. Soc. Symp. Proc.* **2014**, *1757*, 1–6. [CrossRef]
46. Jiménez, A.R.; Klöpsch, R.; Wagner, R.; Rodehorst, U.C.; Kolek, M.; Nölle, R.; Winter, M.; Placke, T. A Step toward High-Energy Silicon-Based Thin Film Lithium Ion Batteries. *ACS Nano* **2017**, *11*, 4731–4744. [CrossRef]
47. Tong, Y.; Xu, Z.; Liu, C.; Zhang, G.; Wang, J.; Wu, Z.G. Magnetic sputtered amorphous Si/C multilayer thin films as anode materials for lithium ion batteries. *J. Power Sources* **2014**, *247*, 78–83. [CrossRef]

48. Huang, Y.; Zeng, Y.; Zhang, Z.; Guo, X.; Liao, M.; Shoud, C.; Huang, S.; Yan, B.; Ye, J. UV-Raman scattering of thin film Si with ultrathin silicon oxide tunnel contact for high efficiency crystal silicon solar cells. *Sol. Energy Mater. Sol. Cells* **2019**, *192*, 154–160. [[CrossRef](#)]
49. Wang, A.; Liu, F.; Wang, Z.; Liu, X. Self-assembly of silicon/carbon hybrids and natural graphite as anode materials for lithium-ion batteries. *RSC Adv.* **2016**, *6*, 104995. [[CrossRef](#)]
50. Mishra, P.; Jain, K.P. First- and second-order Raman scattering in nanocrystalline silicon. *Phys. Rev. B* **2001**, *64*, 73304–73308. [[CrossRef](#)]
51. Abidi, D.; Jusserand, B.; Fave, J.-L. Raman scattering studies of heavily doped microcrystalline porous silicon and porous silicon free-standing membranes. *Phys. Rev. B* **2010**, *82*, 75210–75221. [[CrossRef](#)]
52. Wong, S. Controlling Indentation-Induced Phases of Silicon. Ph.D. Thesis, Australian National University, Canberra, Australia, 2017.
53. Domnich, V.; Gogotsi, Y. *Frontiers of High Pressure Research II: Application of High Pressure to Low-Dimensional Novel Electronic Materials*; Springer: Berlin/Heidelberg, Germany, 2002; pp. 291–302.
54. Hauge, H.I.T.; Verheijen, M.A.; Conesa-Boj, S.; Etzelstorfer, T.; Watzinger, M.; Kriegner, D.; Zardo, I.; Fasolato, C.; Capitani, F.; Postorino, P.; et al. Hexagonal Silicon Realized. *Nano Lett.* **2015**, *15*, 5855–5860. [[CrossRef](#)] [[PubMed](#)]
55. Ge, D.; Domnich, V.; Gogotsi, Y. Thermal stability of metastable silicon phases produced by nanoindentation. *J. Appl. Phys.* **2004**, *95*, 2725–2731. [[CrossRef](#)]
56. Wyckoff, R.W.G. *Crystal Structures*; Interscience Publishers: New York, NY, USA, 1963; Volume 1, pp. 7–83.
57. Kasper, J.S.; Wentorf, R.H. Hexagonal (Wurtzite) Silicon. *Science* **1977**, *197*, 599. [[CrossRef](#)]
58. Yoon, T.; Nguyen, C.C.; Seo, D.M.; Lucht, B.L. Capacity Fading Mechanisms of Silicon Nanoparticle Negative Electrodes for Lithium Ion Batteries. *J. Electrochem. Soc.* **2015**, *162*, A2325–A2330. [[CrossRef](#)]
59. Obrovac, M.N.; Christensen, L. Structural Changes in Silicon Anodes during Lithium Insertion/Extraction. *Electrochem. Solid-State Lett.* **2004**, *7*, A93–A96. [[CrossRef](#)]
60. Dutta, S.; Bhaumik, A.; Wu, K.C.W. Hierarchically porous carbon derived from polymers and biomass: Effect of interconnected pores on energy applications. *Energy Environ. Sci.* **2014**, *7*, 3574–3592. [[CrossRef](#)]
61. Novák, P.; Goers, D.; Spahr, M.E. Carbon Materials in Lithium-Ion Batteries. In *Carbons for Electrochemical Energy Storage and Conversion Systems*; Béguin, F., Frackowiak, E., Eds.; Taylor and Francis Group, LLC: Boca Raton, FL, USA, 2010; pp. 283–285.

**Disclaimer/Publisher’s Note:** The statements, opinions and data contained in all publications are solely those of the individual author(s) and contributor(s) and not of MDPI and/or the editor(s). MDPI and/or the editor(s) disclaim responsibility for any injury to people or property resulting from any ideas, methods, instructions or products referred to in the content.